

Constraining Black Hole Parameters from Shadow and Inner-Shadow Morphology Considering Effects from Thick Disk Accretion Flows

JULIEN A. KEARNS,¹ DOMINIC O. CHANG,^{2,3} DANIEL C. M. PALUMBO,^{3,4} AND SHANE W. DAVIS¹

¹*Department of Astronomy, University of Virginia, Charlottesville, VA, 22904, USA*

²*Department of Physics, Harvard University, Cambridge, MA 02138, USA*

³*Black Hole Initiative At Harvard University, 20 Garden Street, Cambridge, MA 02138, USA*

⁴*Center for Astrophysics, Harvard & Smithsonian, 60 Garden Street, Cambridge, MA 02138, USA*

ABSTRACT

We study the effects of emission geometry on the capability to constrain black hole parameters from measurements of the shadow and inner-shadow of a Reissner-Nordström black hole. We investigate the capability to constrain mass, charge, observer inclination, and emission co-latitude from images of black hole accretion flows that would arise from thick and thin accretion disks. We confirm previous studies that have shown that independent radii measurements of the shadow and inner-shadow can constrain black hole parameters if the viewing inclination is known, but find that it is only possible if the true emission geometry is also assumed. We study the constraining capabilities of the shadow and inner-shadow observations of M87* and Sgr A* like systems within the context of the BHEX and NgEHT future observatories.

1. INTRODUCTION

In 2017, The Event Horizon Telescope Collaboration (EHTC) made observations of the centers of the galaxy M87 and the Milky Way with a global array of radio telescopes utilizing Very Long Baseline Interferometry (VLBI) observing at 1.3 mm wavelengths (EHTC et al. 2019a,b; EHTC et al. 2022a). These observations were used to produce the first pictures of the shadows of black holes M87* and Sgr A* (EHTC et al. (2019a,c); EHTC et al. (2022a,b)). The images depict ring-like features of $\sim 40 \mu\text{as}$ in extent that have asymmetrical brightness distributions and are consistent with previous theoretical predictions of the appearances of black holes (Bardeen 1973; Luminet 1979; Falcke et al. 2000). These observations allowed the collaboration to establish constraints on the mass of M87* (see EHTC et al. 2019d, for their analysis) and the orientation of its spin axis with respect to Earth’s line of sight.

The ring-like features seen in black hole images are predicted to be composed of emission from multiple nested photon rings that converge in shape and size to a critical curve (Johnson et al. 2020; Gralla & Lupsasca 2020). The shape and morphology of photon rings are agnostic to the underlying accretion physics, and are only sensitive to black hole mass, spin and charge (Walia

2024). These features suggest that photon ring measurements could be used to constrain black hole space time parameters. Individual photon rings are, however, likely unresolvable at the current nominal resolution of the instrument (reported to be $\sim 25 \mu\text{as}$ in EHTC et al. 2019a).

Another image feature that has been predicted, but not yet observed, is the black hole inner-shadow. The inner-shadow is associated with the footprint of the jet on the black hole horizon seen at mm wavelengths. Chael et al. (2021) have suggested the inner-shadow could serve as an additional probe of black hole space time properties. Measurements of the inner-shadow would, however, require observations with high dynamic range that is challenging for the current EHT array, but will be possible with upgrades in the near future Johnson et al. (2023) (Johnson et al. 2023; Johnson et al. 2024). Observations of these image features could therefore serve as constraints for measurements of black hole spacetime parameters; and thus understanding how their morphologies are linked to their underlying black hole parameters is relevant.

This work focuses on constraints that can be derived from measurements of the critical curve and inner-shadow around black holes, and how such measurements can be confounded by variations in accretion geometries. We specifically focused on the case of a charged spherically symmetric black hole. Though we do not expect

astrophysical black holes to carry much electric charge, the effects of charge on the size of the black hole shadows and inner-shadows are similar to effects caused by spin. The additional symmetry afforded by our assumption allows for easier interpretation of some of our results.

The outline of this paper is as follows: In section 2, we discuss the theoretical basis for modeling images of accretion flows around spherically symmetric black holes. In section 3, we use this formalism to study the shadow and inner-shadow image features of accretion flows around black holes that are relevant for M87* and Sgr A*, and how they can be used to constrain various spacetime parameters. We also study the confounding effects of non-equatorial emission geometry on parameter inference. Finally we conclude by summarizing our results.

2. RAY TRACING METHOD

Here, we summarize our method for ray tracing surfaces in static, spherically symmetric spacetimes. We will take our observer to be at $r = \infty$. In this work, solving the ray tracing problem amounts to finding the mapping of points in the spacetime to points on an observer's screen through the action of photon geodesics (see Luminet 1979, for an example of a star field around a Schwarzschild black hole).

2.1. Null Geodesics in Spherically Symmetric Black Hole Space Times

We constrain the following discussion to a sub-class of degenerate, static, spherically symmetric, asymptotically flat metrics (see Frolov et al. (2017) for a review on metric classifications based their symmetry structure), described by a line element with ansatz,

$$ds^2 = -f(r) c^2 t^2 + \frac{\dot{r}^2}{f(r)} + r^2 [\dot{\theta}^2 + \sin^2(\theta) \dot{\phi}^2], \quad (1)$$

where t is the time coordinate of the asymptotic observer, r is the areal radius of the space-time, θ and ϕ are the spherical inclination and azimuthal angles. We will take $G = M = c = 1$ hereafter. We use \dot{x} to indicate a derivative of x with respect to the affine parameter λ . The time translation and rotational symmetries of Equation 1 imply that photon geodesics can be fully characterized in terms of a conserved energy,

$$E = f(r) \dot{t}, \quad (2)$$

and azimuthal angular momentum,

$$L = r^2 \sin^2(\theta) \dot{\phi}. \quad (3)$$

We first consider geodesic motion in the equatorial plane. The line element of Equation 1 is then be brought

to the form,

$$\frac{d\phi}{dr} = \pm \frac{b}{\sqrt{R(r)}}, \quad (4)$$

where we have defined the radial potential,

$$R(r) = \frac{E}{L} \sqrt{r^2 \left[r^2 - f(r) \frac{L^2}{E^2} \right]}. \quad (5)$$

The winding angle, ψ , accrued by a photon trajectory can then be written as,

$$\psi(r_s) = \Delta\phi = \int_{r_s}^{\infty} \pm \frac{b}{\sqrt{R(r)}} dr, \quad (6)$$

where \int indicates a path dependent integral, r_s is the radius of emission, b is the impact parameter of the photon, and the \pm indicates whether the radial momentum of the photon is outgoing or ingoing.

Alternatively, we can use the Hamilton-Jacobi Equations (Carter 1968) to bring Equation 1 to the form,

$$\frac{r^2 \left(E^2 - \frac{1}{r^2} \left(\frac{dr}{d\tau} \right)^2 \right)}{f(r)} = \left(\frac{d\theta}{d\tau} \right)^2 + \frac{L^2}{\sin^2 \theta} = Q + L^2, \quad (7)$$

where Q is the Carter integral, and $d\tau = \frac{1}{r^2} d\lambda$ is the Mino-time. This expression can be used to define the integral equations,

$$\frac{d\tau}{dr} = \frac{1}{E^2 \sqrt{r^2 \left[r^2 - \frac{(Q+L^2)}{E^2} f(r) \right]}} \quad (8a)$$

$$\frac{d\tau}{d\theta} = \frac{1}{\sqrt{Q - L^2 \cot^2 \theta}}, \quad (8b)$$

Equation 8a, is of the same form as Equation 5. We can therefore directly relate the Mino-time to the winding angle, and write Equation 8b as,

$$\psi(\theta_s, i) = \int_{\theta_s}^i \pm \frac{E b}{\sqrt{Q - L^2 \cot^2 \theta}} d\theta, \quad (9)$$

where $b = \sqrt{(Q + L^2)}/E$, θ_s is the emission inclination, and i is the observer inclination. It follows that,

$$\psi(r_s) = \psi(\theta_s, \theta_0). \quad (10)$$

The root structure of Equation 6 can be used to broadly classify photon trajectories as either plunging or scattering. Trajectories whose radial potentials have their largest real root behind the horizon (or with no real roots at all) are called “plunging”, and those with their largest real root outside the horizon are “scattering”.

Plunging trajectories can be expressed as monotonic functions in r ,

$$\psi_{\text{plunging}}(r_s) = \int_{r_s}^{\infty} \frac{b}{\sqrt{R(r)}} dr, \quad (11)$$

and thus do not have a path dependent integral. Scattering trajectories, on the other hand, have two possible values of $\phi_{\text{scattering}}$ for each $r > r_t$, where r_t is the largest real root of $R(r)$, and exactly one value of $\phi_{\text{scattering}}$ at $r = r_t$. We can therefore bring $\phi_{\text{scattering}}$ into a path-independent form with an appropriate double covering of the domain. We use the pre-image of a parabola,

$$r = x^2 + \tau. \quad (12)$$

and combine ϕ_{plunging} and $\phi_{\text{scattering}}$ to define,

$$\psi(x_i) = \int_{x_i}^{\infty} \frac{d\phi}{dx} dx \quad (13)$$

where,

$$\frac{d\phi}{dx} = \frac{-2b|x|}{(x^2 + \tau) \sqrt{-\frac{(b^2)(-2+x^2+\tau)}{x^2+\tau}} + (x^2 + \tau)^2}. \quad (14)$$

and,

$$\tau = \begin{cases} 0 & \text{plunging} \\ r_t & \text{scattering} \end{cases}. \quad (15)$$

We specialize to the case of an electrically charged, spherically symmetric black hole described by the Reissner-Nordström solution, (Reissner 1916; Weyl 1917; Nordström 1918). This black hole has a line element given by Equation 1 with,

$$f(r) = 1 - \frac{2M}{r} + \frac{Q^2}{r^2}, \quad (16)$$

and associated radial potential,

$$R(r) = r^2 \left[r^2 - b^2 \left(1 - \frac{2}{r} + \frac{Q^2}{r^2} \right) \right]. \quad (17)$$

This black hole has an outer event horizon at,

$$h = M + \sqrt{M^2 - Q^2} \quad (18)$$

2.2. Observer's Screen Coordinates

We use the coordinates of Bardeen (1973) for the screen of our observer. The horizontal and vertical coordinates, (α, β) , are defined as,

$$x = -\frac{1}{r} \frac{\dot{\phi}}{\dot{t}} = -\frac{L}{E} \frac{1}{\sin i}, \quad \text{and} \quad (19a)$$

$$y = \frac{1}{r} \frac{\dot{\theta}}{\dot{t}} = \frac{1}{E} \sqrt{Q - L^2 \cot i}, \quad (19b)$$

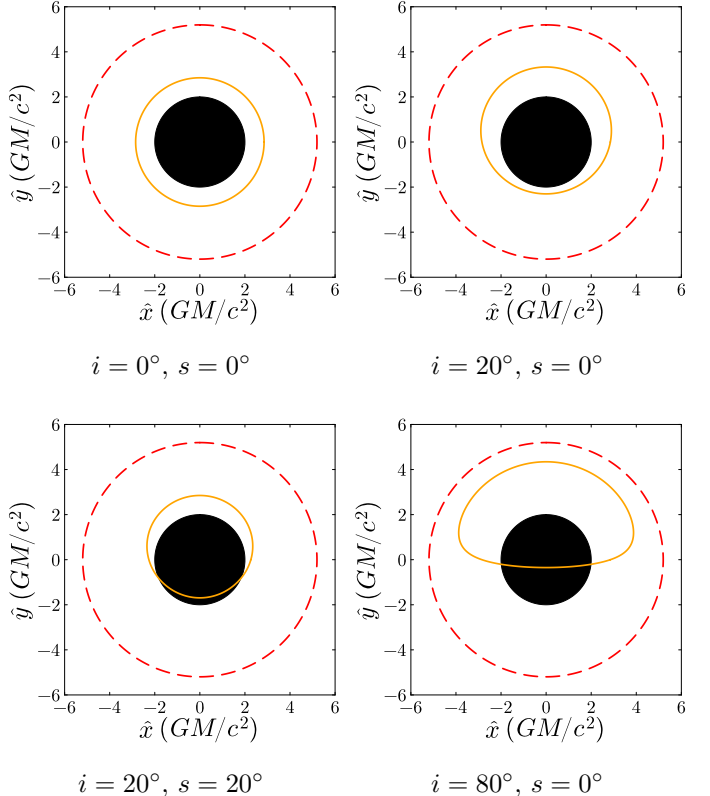


Figure 1. Critical curve (red, dashed lines) and inner-shadow (orange lines) of accretion disks with varying horizon intersection co-latitude around a Schwarzschild black hole as seen by observers at varying inclinations with respect to the symmetry axis of the accretion disk. We show differences in images seen by an observer viewing a thin disk accretion system at inclinations of 20° and 80° with respect to the symmetry axis of the disk. We also show differences in the size of the inner-shadow (orange curve) at emission co-latitudes of 0° and 20° . The un-lensed image of the black hole horizon, a radius of $r_h = 2GM/c^2$, in the absence of gravitational lensing is shown for scale (solid black disk).

where \dot{t} , $\dot{\phi}$ and $\dot{\theta}$ have been evaluated at the asymptotic observer's location. We will also set up polar coordinates on the observer's screen with,

$$b = \sqrt{\alpha^2 + \beta^2}, \quad \text{and} \quad (20a)$$

$$\varphi = \arctan \left(\frac{\beta}{\alpha} \right), \quad (20b)$$

where b is, again, the impact parameter which also serves as the radial coordinate, and φ is the angular coordinate.

2.3. Ray Tracing the Shadow and Inner-Shadow of an Accretion Disk

Black holes produce electromagnetic radiation from the accretion of magnetized plasma flows. These flows

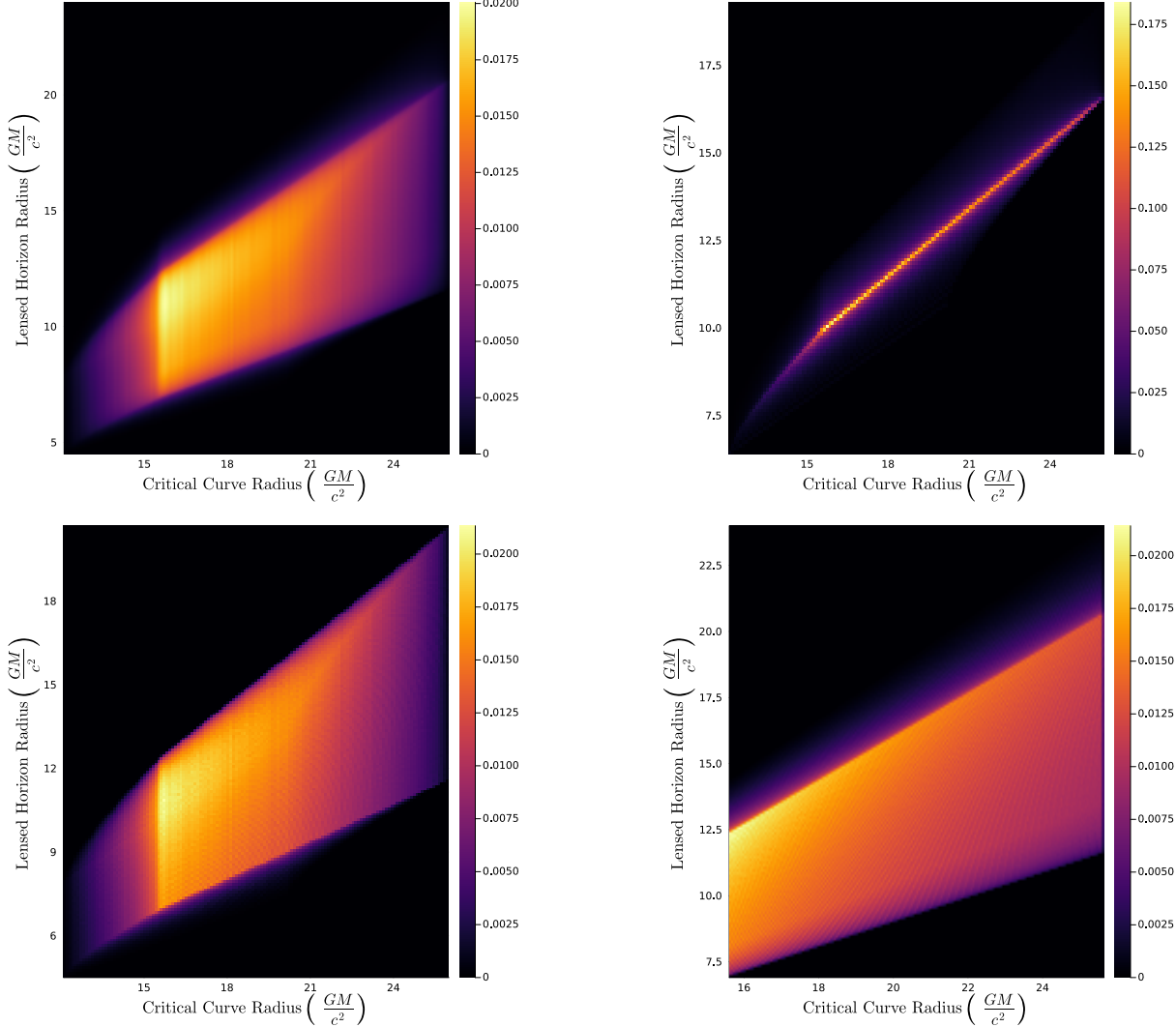


Figure 2. (Top left panel) normalized 2-D density plot of \bar{r}_h and r_c value over $M/D \in [3, 5]$, $q \in [0, 1]$, $s \in [-30^\circ, 30^\circ]$, and $i \in [0^\circ, 85^\circ]$. The top-right, bottom-left and bottom-right panels are the same as the top-left, but after restricting $s = 0$, $i = 0$ and $q = 0$ respectively.

are broadly classified as either cold or hot accretion (Yuan & Narayan 2014), with cold flows being geometrically thin and optically thick, and hot flows being geometrically thick and optically thin. These effects can cause the *appearance* of a black hole accretion disks to vary in thickness (EHTC et al. 2019e), which has been shown to have measurable effects on their images Chang et al. (2024).

Although intrinsic variation in accretion flows can modify the images of accretion disks (See Chang et al. 2025, for an empirical study), there are some features that are believed to be present in every image. Two of these features are the photon ring and the inner-shadow (Cunha & Herdeiro 2020; Johnson et al. 2020; Chael et al. 2021). We will extend the definition of the inner-shadow in the following section to include thick accretion

disks with boundary has an “emission co-latitude” s at the horizon.

2.3.1. The Shadow of the Black Hole

The shadow of a black hole is bounded by the photon ring. The Photon ring is an image feature formed from photons that traverse on nearly bound orbits around unstable maxima of the radial potential. This feature is expected to appear as a bright, sharp ring-like feature in images. The appearance of this feature is determined by the impact parameter, $b = b_c$ and emission radius, r_c that satisfies,

$$R(r_c) = 0 \quad (21a)$$

$$\partial_r R(r_c) = 0 \quad (21b)$$

$$\partial_r^2 R(r_c) < 0. \quad (21c)$$

For the case of a Reisner-Nordstrom black hole [Equation 17](#) gives a photon sphere radius of,

$$p_c(q) = \frac{1}{2} \left(3 + \sqrt{9 - 8q^2} \right), \quad (22)$$

and screen radius of,

$$r_c(q) = \frac{\sqrt{27 - 36q^2 + 8q^4 + (9 - 8q^2)^{\frac{3}{2}}}}{\sqrt{2}\sqrt{1 - q^2}}. \quad (23)$$

2.3.2. Inner-Shadow of a Thick Disk

The inner-shadow corresponds to the image feature where the accretion disk meets the event horizon of the black hole. This feature manifests as a sharp boundary in images where there is no/very little emission seen in its interior. This feature can be thought of the ray traced image of a co-latitude curve on the event horizon of a black hole.

First, we consider observer on the north-pole of the coordinate system viewing a “face-on” accretion disk whose axis-of-symmetry is also coincident with the north-pole. This disk will have a thickness described by an emission co-latitude, $s \geq 0$. The scale height relates the two disk boundaries to the coordinate inclination by,

$$s = \pi/2 \mp \theta_s, \quad (24)$$

where θ_s is the inclination angle of the disk’s boundary, and the \mp indicates which boundary is being considered. In this case, the emission co-latitude s of the disk is directly related to the winding angle by¹,

$$\psi(s) = \pi/2 \mp s \quad (25)$$

for photons emitted with $\dot{\theta}_s < 0$, and

$$\psi(s) = (3\pi/2 \pm s) \quad (26)$$

for trajectories photons emitted with $\dot{\theta}_s > 0$ ([Kocherlakota et al. 2024](#)). We can label points on one of the disk boundaries uniquely with combinations of (r, ϕ) . This choice of coordinates allows us to map points on

the disk boundary to the observer’s screen through the relationships,

$$\psi(s) = \psi(r_s), \quad \text{and} \quad (27a)$$

$$\varphi|_{i=0} = \phi. \quad (27b)$$

We ray trace this surface with the `Roots.jl` package ([Verzani 2020](#)) by solving [Equation 27a](#) numerically.

In general, an accretion disk will have a axis-of-symmetry with arbitrary tilt with respect to the observer’s line-of-sight. We construct the ray traced solution by again considering a disk whose symmetry axis is aligned with the north-pole of the coordinate system, but now with an observer sitting at an inclination of i . Taking [Equation 9](#), [Equation 19](#) and [Equation 20](#) with $\theta_s = \pi/2 - s$ gives,

$$\psi_{ss}(\varphi, \theta_s) = \begin{cases} -\psi(\varphi, \theta_s, i), & \text{if } \psi(\varphi, \theta_s) < 0 \\ \pi - \psi(\varphi, \theta_s), & \text{if } \psi(\varphi, \theta_s) \geq 0, \end{cases} \quad (28)$$

with,

$$\psi(\varphi, \theta_s) = \arctan \left[\frac{\cot \theta_s}{\sqrt{1 - \cos^2 \varphi \csc^2 \theta_s \sin^2 i}} \right] - \arctan \left[\frac{1}{\tan i \sin \varphi} \right]. \quad (29)$$

We again ray trace this surface with the `Roots.jl` by numerically solving the equation,

$$\psi_{ss}(\varphi, \theta_s, i) = \psi(r_h), \quad (30)$$

where r_h is the radius of the horizon.

3. SPACETIME CONSTRAINTS FROM MEASUREMENTS OF THE SHADOW AND INNER-SHADOW FEATURES

In this section, we study the capability for measurements of the size and shape of the shadow and inner-shadow to constrain black hole mass, charge q , observer inclination i and emission co-latitude between the accretion disk and the horizon s , as measured in the lab frame. We also show, through examples, how measurement uncertainties and model assumptions can affect the quality of our constraints. We calculate uncertainties that are consistent with the potential resolving power of the future ngEHT and BHEX missions when they will observe M87* and Sgr A* ([Johnson et al. 2023; Johnson et al. 2024](#)). For studies where the known mass is assumed, we use a nominal mass-to-distance ratio of $3.78\mu\text{as}$, though we note that a change in the mass-to-distance ratio of the black hole is equivalent to applying

¹ Only the direct, $n = 0$, images of the disk are relevant for defining the inner-shadow.

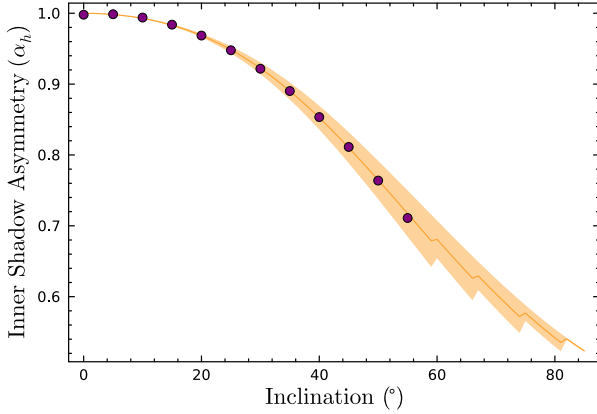


Figure 3. α_h vs. i , for a Reisner-Nordstrom black hole over a range of charges $q \in [0, 1]$ and emission co-latitudes $s \in [0^\circ, 30^\circ]$. We find a best fit quadratic curve $\alpha_h(i) = -1 \times 10^{-4}(i - 3.1)^2 + 1$ that is traced with purple points for values of $i \in [0^\circ, 50^\circ]$. The orange region represents the range of inner-shadow asymmetry values that are consistent with each inclination parameter. The thinness of the orange region implies a strong relationship between α_h and i .

a uniform scaling to the sizes of the shadow and inner-shadow.

The morphology of the shadow and inner-shadow will, in general, vary with respect to the mass-to-distance ratio, q , i and s . Since the size of the shadow is completely determined by Equation 23, it will always appear circular in shape, and its size will only depend on q (see Figure 1). The appearance of the inner-shadow, on the other hand, varies with respect to all these parameters. In order to quantify this dependency, we define a_h and b_h as the inner-shadow principle axes, with a_h being the longest horizontal cross-section and b_h the longest vertical. These quantities are used to define the average size of the inner-shadow as,

$$\bar{r}_h = \frac{a_h + b_h}{2}, \quad (31)$$

and the asymmetry, α_h as,

$$\alpha_h = \frac{a_h}{b_h}. \quad (32)$$

Figure 2 explores the space of degeneracy in sections of the M/D , i , q , and s parameter space. We note that the narrowness of the histogram support in the top-right panel of Figure 2, when compared to the other panels, suggest that \bar{r}_h and r_c are more closely related when s is known. This behavior suggests that emission geometry will play an important role in measurement uncertainty.

3.1. (Sgr A* like system) Measurement of Charge, Inclination and Scale Height

We study how measurements of the shadow and inner-shadow morphology could be used to constrain black hole charge, q , and viewing inclination, i and emission co-latitude s . We use a black hole that is assumed to have an accurate measurement of its M/D , but is uncertain in its emission geometry, inclination and charge; as is the case of Sgr A* (EHTC et al. 2022c; Gillessen et al. 2009). We will assume a known M/D of $3.78 \mu\text{as}$, though the main takeaways of our results are generic and can be re-scaled for black holes of other known M/D .

First, we show the relationship between α_h and observer inclination in Figure 3 for different values of q . The top panel shows a monotonically decreasing trend of asymmetry, α_h , with inclination. This trend is very well described by a parabola for values of $i \in [0^\circ, 50^\circ]$. At most, we find a fractional deviation of 4% from this trend on all values of $q \in [0, 1]$ and $s \in [0^\circ, 30^\circ]$. The insensitivity of this behavior to changing values in charge and emission geometry reveals a reliable way to discern the accretion disk's viewing inclination from inner-shadow asymmetry.

The behavior of r_h is more variable in comparison to α_h . The left panel of Figure 4 shows the relationship between \bar{r}_h , charge and inclination for an inner shadow with co-latitude of $s = 0$. We find that \bar{r}_h grows non-linearly with decreasing charge and increasing inclination. Similarly, the right panel of Figure 4 shows the relationship between \bar{r}_h , charge and emission co-latitude at a fixed inclination of $i = 0^\circ$. We see that for most values of q , \bar{r}_h grows at a nearly linear rate with $\sim \sqrt{\Delta q^2 + \Delta s^2}$ (see figure Figure 4).

Figure 5 shows an example of how an accurate measurement of \bar{r}_h constrains regions of parameter space under various assumptions. The left panel shows how an assumption of a known s constrains a region of space between q and i . In this example, a perfect measurement constrains q between the values of $[0.16, 0.75]$. However, the constraint region is heavily dependent on measurement quality. We show, for example, how an error of 1% uncertainty, chosen to be consistent with the theoretical resolving power of BHEX (Johnson et al. 2024), could prevent the establishment of a lower bound on q . The contour spacings in the top panel of Figure 4 indicates that measurement uncertainty in \bar{r}_h introduces greater degeneracies when the black hole is of lower charge or when viewed at lower inclinations. The right panel shows the related problem of constraining q and s with a measurement of \bar{r}_h assuming a known i constraint. Because r_h increases radially out from the plot, a 1% and 5% traces out bands of near constant width.

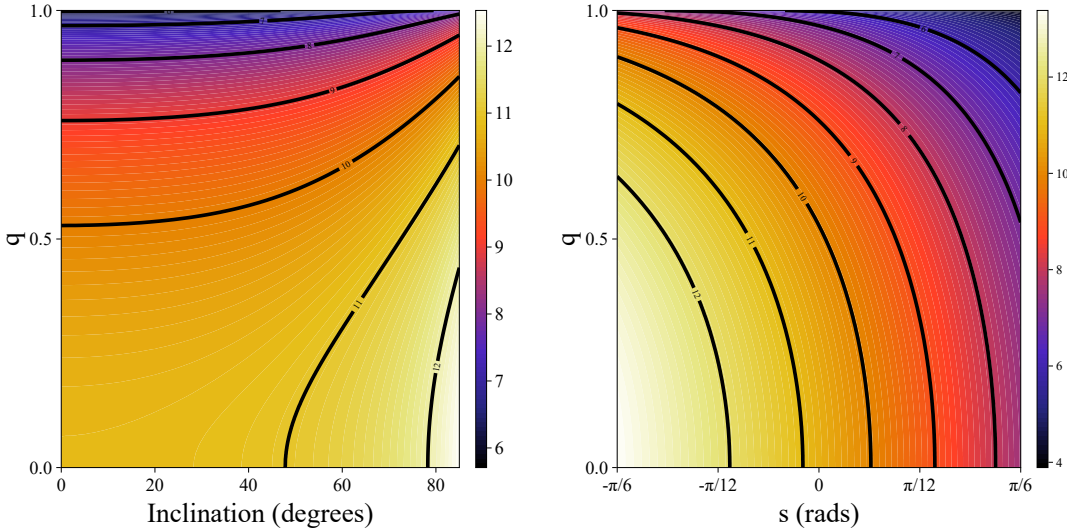


Figure 4. (Left panel) Filled contour plot of all potential \bar{r}_h values across different inclinations and charges. Our values are chosen for a black hole with mass-to-distance ratio $M/D = 3.78 \mu\text{as}$ and emission co-latitude $s = 0$. Isoradial contours of \bar{r}_h at whole number intervals are shown in black. (Right panel) Filled contour map of all potential \bar{r}_h values across different emission co-latitudes and charges of a black hole with mass-to-distance ratio $M/D = 3.78 \mu\text{as}$ and viewing inclination $i = 0$. Although only positive co-latitudes are relevant for observations, we plot values of \bar{r}_h for the range $s \in [-30^\circ, 30^\circ]$ to help illustrate general trends. (Bottom panel) Example of constraints made on black hole viewing inclination, i , and charge, q , from measurement of the average radius of the inner-shadow, \bar{r}_h . The measurement shown is for a black hole with true parameters of $q = 0.2$ and $i = 20^\circ$. A measurement of r_c could be used to establish an independent constraint on charge (horizontal black line). The gray region covers a 1% uncertainty region for the value of \bar{r}_h .

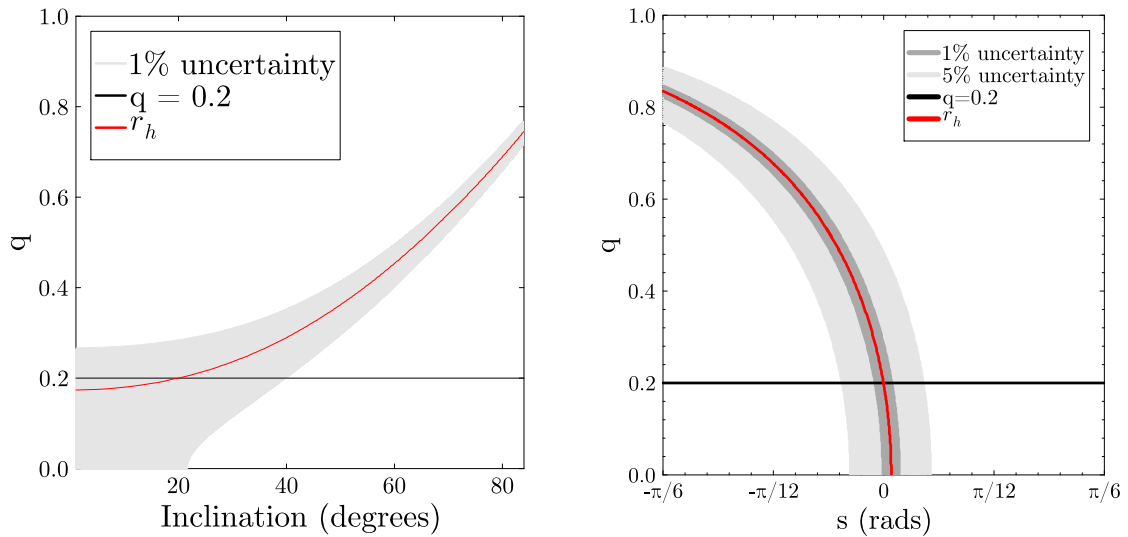


Figure 5. (Left) Filled contour map of all potential \bar{r}_h values across different emission co-latitudes and charges of a black hole with mass-to-distance ratio $M/D = 3.78 \mu\text{as}$ and viewing inclination $i = 0$. Isoradial contours of \bar{r}_h at whole number intervals are shown in black. (Right) Example of constraints on black hole emission co-latitude, s , and charge, q , from measurement of the average radius of the inner-shadow, \bar{r}_h . The measurement shown is for a black hole with true parameters of $q = 0.2$ and $s = 0^\circ$. A measurement of \bar{r}_c could be used to establish an independent constraint on charge (horizontal black line). The dark gray band shows the 1% uncertainty region and the light gray band shows the 5% uncertainty region for our calculation of \bar{r}_h .

3.2. (M87* like system) Measurements of Charge and Mass

Here we study the ability to constrain q and M/D from measurements of \bar{r}_h and r_c , under the assumption of an accurate measurement i . Such is the case of M87* where the mass of the system may not be well constrained, but where measurements of the large scale jet can be used to infer the accretion disk's orientation (Walker et al. 2018; EHTC et al. 2019e). A measurement with these quantities will, however, generally require an additional assumption of the co-latitude at which the accretion disk meets the black hole horizon. From this motivation, we also study the effects of an incorrect assumptions of s on these measurements.

The top panel of Figure 6 shows how a constraint on q and M/D could be made from measurements of \bar{r}_h and r_c where we have assumed the correct value of $s = 0$. We note that this behavior mirrors the results of Chael et al. (2021), which uses similar measurements to constrain a Kerr black hole's mass and spin. In contrast, the bottom panel illustrates the confounding effect that false assumptions on emission geometry can have on parameter inference of these quantities. This consideration contrasts the previous study which assumed equatorial emission. In general, dynamical models of the inner accretion-flows of Sgr A* and M87* often feature emission that is off the equatorial plane which may affect the inner shadow morphology (Chang et al. 2024; EHTC et al. 2019e).

In the bottom panel of Figure 6, an inference is made on q and M/D assuming that the accretion disk meets the horizon in the equatorial plane at $s = 0$. However, the true model is generated with a small emission co-latitude of $s = 5^\circ$. We find that an incorrect assumption in emission co-latitude can introduce biases that translate the \bar{r}_h curve in the q vs. M/D parameter space. Depending on the size of the uncertainty region for \bar{r}_h and r_c , estimated parameters may be incorrectly constrained to a region translated away from the real physical values that produce observed image features. In the case of a small uncertainty region there may be no overlap at all, thus yielding an inconclusive parameter estimation. An inconclusive result would signify that the assumption of an equatorial model is incorrect. In other words, the requirement that \bar{r}_h and r_c curves intersect establishes a range of possible s values.

4. CONCLUSION

We used explorations of numerical Reissner-Nordström black hole models to reveal connections between the morphology of two key image features: the black hole shadow and inner-shadow and constraints on

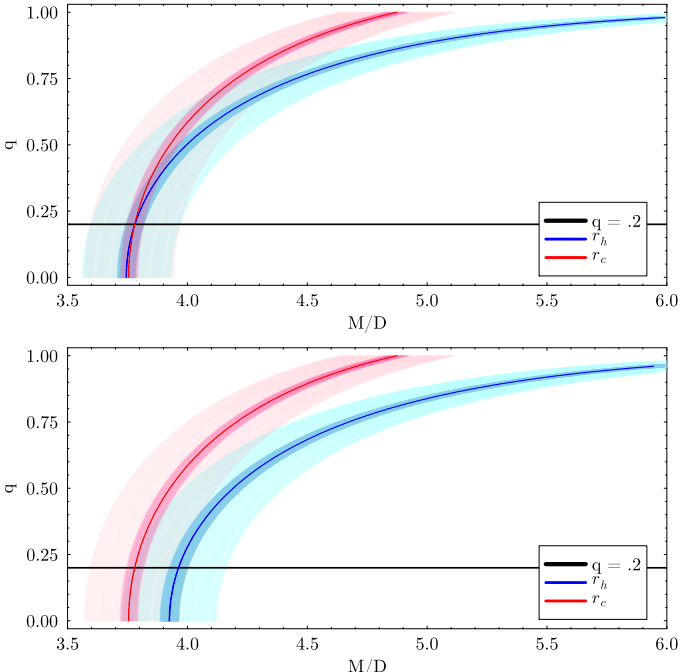


Figure 6. The effects of assumptions on emission geometry on M/D and q constraints. Constraints are made from independent measurements of \bar{r}_h and r_c for a black hole with true parameters of $q = .2$, $M/D = 3.78$ and $s = 0^\circ$. The blue and pink bands represent regions of measurement uncertainty in \bar{r}_h and r_c with thinner bands filling the 1% uncertainty region and the wider bands filling the 5% uncertainty region. The top panel shows the constraints that are made if the emission geometry is correctly assumed, $s = 0$. The bottom panel shows the attempted constraints made if an incorrect assumption is made of the emission geometry's co-latitude, (a truth of $s = 5^\circ$ but assumed to be $s = 0^\circ$). The effect of the incorrect assumption on s is to shift the \bar{r}_h curve to the right towards higher M/D .

various black hole parameters (i , q , s and M/D). Constraints derived from these image features are driven by their relativistic phenomenology. The inner-shadow is bounded by the image of where the accretion disk meets the black hole horizon. We find that the asymmetry, α_h , of the inner-shadow is dependent on the viewing inclination, i , of the observer, and its area, and thus the average radius on the screen, \bar{r}_h , decreases with increasing charge for any constant mass-to-distance ratio, M/D . The case is the same for the shadow, whose radius, r_c , is determined by the critical-curve radius.

We find that q and M/D affect both r_h and r_c , whereas emission co-latitude, s , and i only affect r_h . We confirmed that independent radii measurements of the shadow and inner-shadow can constrain the mass and charge of a target Reissner-Nordström black hole with known viewing inclination for an M87* like system, but only if the near horizon emission geometry is known. We

find that fits of \bar{r}_h to black hole accretion systems with even small deviations from truth in the assumed value of s can lead to false constraints on mass and charge. These results complicate previous studies that derived a unique constraint under the assumption of equatorial emission (Chael et al. 2021). We find that these conclusions are also relevant for Sgr A* like systems where M/D is well known, but the inclination is not.

ACKNOWLEDGMENTS

Julien Kearns was supported by the NSBP/SAO EHT Scholars program. Support for this work was provided by the NSF through grant AST-1952099. We acknowledge financial support from the National Science Foundation (AST-2307887). This publication is funded in part by the Gordon and Betty Moore Foundation, Grant GBMF-12987. This work was supported by the Black Hole Initiative, which is funded by grants from the John Templeton Foundation (Grant #62286) and the Gordon and Betty Moore Foundation (Grant GBMF-8273)—although the opinions expressed in this work are those of the author(s) and do not necessarily reflect the views of these Foundations.

REFERENCES

Bardeen, J. M. 1973, in Black Holes (Les Astres Occlus), 215–239

Carter, B. 1968, Phys. Rev., 174, 1559, doi: [10.1103/PhysRev.174.1559](https://doi.org/10.1103/PhysRev.174.1559)

Chael, A., Johnson, M. D., & Lupsasca, A. 2021, The Astrophysical Journal, 918, 6, doi: [10.3847/1538-4357/ac09ee](https://doi.org/10.3847/1538-4357/ac09ee)

Chang, D. O., Johnson, M. D., & Tiede, P. 2025, Astrophys. J. Lett., 989, L1

Chang, D. O., Johnson, M. D., Tiede, P., & Palumbo, D. C. M. 2024, The Astrophysical Journal, 974, 143, doi: [10.3847/1538-4357/ad6b28](https://doi.org/10.3847/1538-4357/ad6b28)

Cunha, P. V. P., & Herdeiro, C. A. R. 2020, Phys. Rev. Lett., 124, 181101, doi: [10.1103/PhysRevLett.124.181101](https://doi.org/10.1103/PhysRevLett.124.181101)

EHTC, Akiyama, K., Alberdi, A., et al. 2019a, The Astrophysical Journal Letters, 875, L1, doi: [10.3847/2041-8213/ab0ec7](https://doi.org/10.3847/2041-8213/ab0ec7)

—. 2019b, The Astrophysical Journal Letters, 875, L2, doi: [10.3847/2041-8213/ab0c96](https://doi.org/10.3847/2041-8213/ab0c96)

—. 2019c, The Astrophysical Journal Letters, 875, L4, doi: [10.3847/2041-8213/ab0e85](https://doi.org/10.3847/2041-8213/ab0e85)

—. 2019d, The Astrophysical Journal Letters, 875, L6, doi: [10.3847/2041-8213/ab1141](https://doi.org/10.3847/2041-8213/ab1141)

—. 2019e, The Astrophysical Journal Letters, 875, L5, doi: [10.3847/2041-8213/ab0f43](https://doi.org/10.3847/2041-8213/ab0f43)

EHTC, Akiyama, K., Alberdi, A., et al. 2022a, ApJL, 930, L12, doi: [10.3847/2041-8213/ac6674](https://doi.org/10.3847/2041-8213/ac6674)

—. 2022b, ApJL, 930, L14, doi: [10.3847/2041-8213/ac6429](https://doi.org/10.3847/2041-8213/ac6429)

—. 2022c, ApJL, 930, L17, doi: [10.3847/2041-8213/ac6756](https://doi.org/10.3847/2041-8213/ac6756)

Falcke, H., Melia, F., & Agol, E. 2000, ApJL, 528, L13, doi: [10.1086/312423](https://doi.org/10.1086/312423)

Frolov, V. P., Krtouš, P., & Kubizňák, D. 2017, Living Reviews in Relativity, 20, doi: [10.1007/s41114-017-0009-9](https://doi.org/10.1007/s41114-017-0009-9)

Gillessen, S., Eisenhauer, F., Fritz, T. K., et al. 2009, ApJL, 707, L114, doi: [10.1088/0004-637X/707/2/L114](https://doi.org/10.1088/0004-637X/707/2/L114)

Gralla, S. E., & Lupsasca, A. 2020, Phys. Rev. D, 101, 044031, doi: [10.1103/PhysRevD.101.044031](https://doi.org/10.1103/PhysRevD.101.044031)

Johnson, M. D., Doeleman, S. S., Gómez, J. L., & Broderick, A. E. 2023, Galaxies, 11, doi: [10.3390/galaxies11050092](https://doi.org/10.3390/galaxies11050092)

Johnson, M. D., Lupsasca, A., Strominger, A., et al. 2020, Science Advances, 6, eaaz1310, doi: [10.1126/sciadv.aaz1310](https://doi.org/10.1126/sciadv.aaz1310)

Johnson, M. D., Akiyama, K., Baturin, R., et al. 2024, in Society of Photo-Optical Instrumentation Engineers (SPIE) Conference Series, Vol. 13092, Space Telescopes and Instrumentation 2024: Optical, Infrared, and Millimeter Wave, ed. L. E. Coyle, S. Matsuura, & M. D. Perrin, 130922D, doi: [10.1117/12.3019835](https://doi.org/10.1117/12.3019835)

Kocherlakota, P., Rezzolla, L., Roy, R., & Wielgus, M. 2024, MNRAS, 531, 3606, doi: [10.1093/mnras/stae1321](https://doi.org/10.1093/mnras/stae1321)

Luminet, J. P. 1979, A&A, 75, 228

Nordström, G. 1918, Koninklijke Nederlandse Akademie van Wetenschappen Proceedings Series B Physical Sciences, 20, 1238

Reissner, H. 1916, Annalen der Physik, 355, 106, doi: <https://doi.org/10.1002/andp.19163550905>

Verzani, J. 2020, Roots.jl: Root finding functions for Julia, <https://github.com/JuliaMath/Roots.jl>

Walia, R. K. 2024, Physical Review D, 110, doi: [10.1103/physrevd.110.064058](https://doi.org/10.1103/physrevd.110.064058)

Walker, R. C., Hardee, P. E., Davies, F. B., Ly, C., & Junor, W. 2018, ApJ, 855, 128, doi: [10.3847/1538-4357/aaafcc](https://doi.org/10.3847/1538-4357/aaafcc)

Weyl, H. 1917, Annalen der Physik, 359, 117, doi: <https://doi.org/10.1002/andp.19173591804>

Yuan, F., & Narayan, R. 2014, ARA&A, 52, 529,
doi: [10.1146/annurev-astro-082812-141003](https://doi.org/10.1146/annurev-astro-082812-141003)